Field Test Results of GNSS-denied Inertial Navigation aided by Phased-array Radio Systems for UAVs

Kristoffer Gryte Torleiv H. Bryne Sigurd M. Albrektsen Tor A. Johansen
Center for Autonomous Marine Operations and Systems
Department of Engineering Cybernetic
Norwegian University of Science and Technology
Trondheim, Norway

***Abstract*— Unmanned aerial vehicles (UAVs) often depend on global navigation satellite systems (GNSS) and magnetic compasses for navigation, making them exposed to malicious attacks and sensitive to magnetic anomalies, while restricting operations to within GNSS coverage. By rather relying on inertial navigation aided by spherical position measurements from a phased-array radio system (PARS), these vulnerabilities are avoided. The navigation system relies on a multiplicative extended Kalman filter for state corrections, and on outlier rejection to mitigate effects of radio reflections. Field testing shows that, despite the higher levels of noise in the PARS signal, the PARS-based position, velocity and attitude estimates are satisfactory when compared to the autopilot based attitude and velocity and the real-time kinematic (RTK) GNSS position reference solution.**

I. Introduction

Global navigation satellite systems (GNSS) are the primary positioning solution for unmanned aerial vehicles (UAVs), due to its attractive features: global coverage, lightweight receivers, high accuracy and low cost. However, GNSS are not free of potential issues. Due to the low signal-to-noise ratio (SNR) of GNSS, such position systems are prone to both jamming [1] and spoofing [2]. One alternative to overcome this is to use redundant positioning systems. This also helps mitigate single point of failure, either hardware or software, in GNSS user equipment, or problems related to the GNSS signals (signal objection, solar winds, etc.)[3], preventing the GNSS positioning service to work as intended. With more frequent use of UAVs, the need for alternatives to GNSS becomes more pressing, to allow safe, continuous operation of such systems.

During the past few years, phased-array radio systems (PARS) have been demonstrated on small UAVs as an redundant positioning system [4]. PARS' primary usage is as a high bandwith radio communication tool. In a UAV context this can involve providing the user with telemetry data, including a live video stream[5]. However, since such systems utilize electronic beamforming, they also provide the user with information which can be used to deduce position of the UAV radio relative the ground station [6]. This system complements the security vulnerability aspect of GNSS solutions through its high signal-to-noise ratio, its use of encrypted communication, in addition to the aforementioned redundancy as it is independent of GNSS. It does, however, require radio line-of-sight, and ordinarily has lower accuracy than GNSS solutions. Horizontal PARS-based position accuracy has typically been reported up to ten times lower than that obtained with the Global Positioning System (GPS) standard position service (SPS) [4], [6], [7], depending on range.

In UAV flight, knowledge of the attitude and velocity of the aircraft is, in addition to position, necessary for the flight controller. This, combined with the lower position accuracy of PARS compared to GNSS, motivates the usage of an PARS aided inertial navigation system (INS), which is based on mechanization of inertial sensors such as accelerometers (ACC) and angular rate sensors (ARS), to filter the PARS position while obtaining estimates of the velocity and attitude.

In the light of advances in small UAVs, and in the imminent dangers of cyber-security and GNSS denial of service, PARS for navigation of small UAVs has been an ongoing research topic by the authors of this paper. Notable previous work include a nonlinear observer for aided INS, using PARS, barometer, compass and and IMU [6], and a robust UAV navigation system using GNSS in combination with PARS, for spoofing detection and mitigation[7].

In this work the aiding on the INS is implemented using an indirect multiplicative extended Kalman filter (MEKF)[8]. This is motivated by the desire to couple estimation error between the translational and rotational kinematics in a single state space, such that cross covariance between all states can be exploited when applying aiding corrections based on the the PARS measurements. Previous flights [6], [7] included long passes over water, and contained outliers presumed to come from radio reflections from the water surface. Motivated by this, the present work investigated if the outliers persists also when flying over land, while extending the navigation system to also include outlier rejection. Furthermore, in this work, the compass, which is considered an unreliable

This work was partly supported by the Norwegian Research Council and through the *Hybrid Operations in Maritime Environments* program at MAROFF together with the FRINATEK projects *Low-Cost Integrated Navigation Systems Using Nonlinear Observer Theory* and *Multi-stage global sensor fusion for navigation using nonlinear observers and eXogenous Kalman filter*, and the Center of *Autonomous Marine Operations and Systems* (AMOS AMOS) at the Norwegian University of Science and Technology (NTNU) (grants no. 269480, 221666, 250725 and 223254).
Corresponding Author: gryte@ieee.org

yet common sensor for heading estimation, is not needed since the heading is observable in the presented error-state equations, given enough excitation. The results presented in this paper are based on an online implementation, contrary to previous work, that have presented proofs-of-concept by post-processing the data.

The paper starts by presenting some notational and mathematical preliminaries in Section II, before explaining the measurement used in the presented PARS, and their equations, in Section III. Section IV explains how these measurements are combined, using a Multiplicative Extended Kalman Filter, to provide estimates of the position, attitude and velocity of the vehicle. Section V presents the hardware and software used to implement the INS in a real-time environment and to obtain the experimental results presented in Section VI.

II. Preliminaries

Before presenting the PARS-based navigation system we state some preliminaries on mathematical mathematical notations, attitude representations, used coordinate systems and the strapdown equations used.

A. Notation

The Euclidean vector norm is denoted $\| \cdot \|_2$, the $n \times n$ identity matrix is denoted $\boldsymbol{I}_n$, while the transpose of a vector or a matrix is denoted $(\cdot)^\mathsf{T}$. Coordinate frames are denoted with $\{\cdot\}$. $\boldsymbol{S}(\cdot) \in SS(3)$ represents the skew symmetric matrix such that $\boldsymbol{S}(z_1)z_2 = z_1 \times z_2$ for two vectors $z_1, z_2 \in \mathbb{R}^3$. $z = (z_1; z_2; \ldots; z_n)$ denotes a vector of stacked column vectors $z_1, z_2, \ldots z_n$. Furthermore, error variables are represented with with $\delta\star$, where $\star$ is the variable placeholder. Partial derivatives are denoted with $\partial \star_a / \partial \star_b$. In addition, $z^a_{bc} \in \mathbb{R}^3$ denotes a vector z, to frame $\{c\}$, relative $\{b\}$, decomposed in $\{a\}$. The $\text{diag}(\star_1, ..., \star_n)$ function places the n arguments on the diagonal of a square matrix. Furthermore, T_s represent the sampling time or step length in numerical integration methods.

B. Attitude representations and relationships

The primary attitude representation in this article is the unit quaternion, using the Hamiltonian representation. For rotations from some frame γ to another frame β, the unit quaternion is given as

$$\boldsymbol{q}^\gamma_\beta = \begin{pmatrix} q_s \\ \boldsymbol{q}_v \end{pmatrix} = \begin{pmatrix} q_s \\ q_x \\ q_y \\ q_z \end{pmatrix} \in Q \tag{1}$$

where the set Q is defined according to [9] as

$$Q := \{\boldsymbol{q}^\gamma_\beta \mid (\boldsymbol{q}^\gamma_\beta)^\mathsf{T} \boldsymbol{q}^\gamma_\beta = 1, \boldsymbol{q}^\gamma_\beta = (q_s; \boldsymbol{q}_v), q_s \in \mathbb{R}^1, \boldsymbol{q}_v \in \mathbb{R}^3\} \tag{2}$$

Using Gade's notation [10], the quaternion can be used to calculate rotation matrix, $\boldsymbol{R}_{\gamma\beta} \in SO(3)$,

$$\boldsymbol{R}_{\gamma\beta}(\boldsymbol{q}^\gamma_\beta) = \left(q_s - \boldsymbol{q}_v^\mathsf{T} \boldsymbol{q}_v\right) \boldsymbol{I}_3 + 2q_s \boldsymbol{S}(\boldsymbol{q}_v) + 2\boldsymbol{q}_v \boldsymbol{q}_v^\mathsf{T}, \tag{3}$$

as in e.g. [8, Eq. (4)] and [11, App. D.2].

The Hamiltonian quaternion product, denoted $\otimes$, is given such that

$$\boldsymbol{q}_3 = \boldsymbol{q}_1 \otimes \boldsymbol{q}_2 \quad = \begin{pmatrix} q_{1_s} q_{2_s} - \boldsymbol{q}_{1_v}^\mathsf{T} \boldsymbol{q}_{2_v} \\ q_{1_s} \boldsymbol{q}_{2_v} + q_{2_s} \boldsymbol{q}_{1_v} + \boldsymbol{S}\left(\boldsymbol{q}_{1_v}\right) \boldsymbol{q}_{2_v} \end{pmatrix}, \tag{4}$$

[11, App. D.2]. Moreover, the kinematic equation of a given unit quaternion $\boldsymbol{q}_1$ is given as

$$\dot{\boldsymbol{q}}_1 = \frac{1}{2} \boldsymbol{q}_1 \otimes \bar{\omega} = \frac{1}{2} \boldsymbol{\Omega}(\omega) \boldsymbol{q}_1 \tag{5}$$

where $\bar{\omega} = (\boldsymbol{0}; \omega)$ and

$$\boldsymbol{\Omega}(\omega) = \begin{pmatrix} 0 & -\omega^\mathsf{T} \\ \omega & -\boldsymbol{S}(\omega) \end{pmatrix}, \tag{6}$$

whereas, the quaternion conjugate is denoted as

$$\boldsymbol{q}^* = \begin{pmatrix} p_s, & -\boldsymbol{q}_v \end{pmatrix}^\mathsf{T}. \tag{7}$$

In addition, to the unit quaternion, the Euler angles (roll, pitch and yaw) are given as

$$\boldsymbol{\Theta} = \begin{pmatrix} \phi, & \theta, & \psi \end{pmatrix}^\mathsf{T}. \tag{8}$$

In this paper the attitude error is denoted $\delta\boldsymbol{q}$ and relates to the true attitude $\boldsymbol{q}$ and the INS attitude $\boldsymbol{q}_{\text{ins}}$ through

$$\boldsymbol{q} = \boldsymbol{q}_{\text{ins}} \otimes \delta\boldsymbol{q}, \tag{9}$$

such that

$$\delta\boldsymbol{q} = \boldsymbol{q}^*_{\text{ins}} \otimes \boldsymbol{q}. \tag{10}$$

Finally, the chosen three-dimensional attitude error parameterization of $\delta\boldsymbol{q}$ is four times the Modified Rodrigues Parameters (MRP)

$$\delta\boldsymbol{a} = 4\delta\boldsymbol{a}_{\text{mrp}} = 4\frac{\delta\boldsymbol{q}_v}{1 + \delta q_s} \tag{11}$$

as given in [8].

C. Coordinate Frames

This paper considers three coordinate frames. The first is an Earth-fixed, non-rotating North East Down (NED) frame, denoted $\{n\}$. The second coordinate system is the BODY reference frame, denoted $\{b\}$, respectively. The integrated INS of this article is using this NED frame as navigation frame. The simplification is motivated by the accuracy of the PARS portioning [4] is approximately ten times lower than that of GNSS SPS. This results in the accuracy of the positioning system being much more significant than the assumed simplification of a Earth-fixed, non-rotating NED frame. In addition, the in-run ARS bias stability of MEMS IMUs is typically one order of magnitude or higher than the Earth's rate of rotation. Moreover, the NED directions are respectively denoted N, E, D. See Fig. 1 for details. The third coordinate system is the PARS radio coordinate system, denoted $\{r\}$, which is aligned with the PARS ground station. This coordinate system is a rotated NED frame as can be seen in Fig. 2.

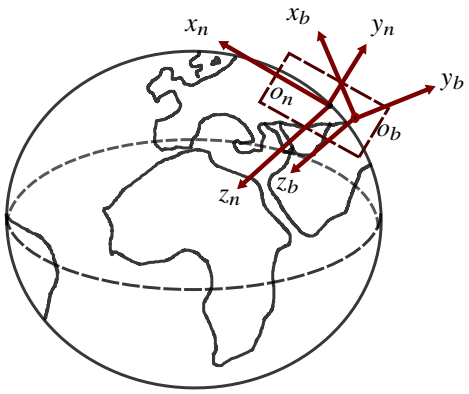

Fig. 1: Definitions of the BODY the NED coordinate frames.

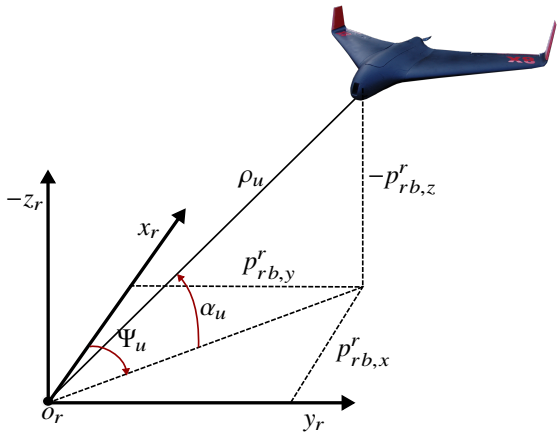

Fig. 2: Range/bearing/elevation measurements. $\{r\}$ and $\{b\}$ denotes the radio and the BODY frame, respectively.

D. Kinematics – Strapdown equations

The position and linear velocity of the BODY frame relative the NED frame are represented as $\boldsymbol{p}^n_{nb} \in \mathbb{R}^3$, $\boldsymbol{v}^n_{nb} \in \mathbb{R}^3$ in the NED frame, as indicated by the superscript n. The attitude between the BODY and the NED frame is given as the unit quaternion $\boldsymbol{q}^n_b$, while the angular velocity of BODY w.r.t to NED is given as $\boldsymbol{\omega}^b_{nb} \in \mathbb{R}^3$, while the gravity vector is given as $\boldsymbol{g}^n_b = (0; 0; g)$. With this stated, the resulting stapdown equations follows

$$\dot{\boldsymbol{p}}^n_{nb} = \boldsymbol{v}^n_{nb} \tag{12}$$

$$\dot{\boldsymbol{v}}^n_{nb} = \boldsymbol{R}_{nb}(\boldsymbol{q}^n_b)\boldsymbol{f}^b_{nb} + \boldsymbol{g}^n_b \tag{13}$$

$$\dot{\boldsymbol{q}}^n_b = \frac{1}{2}\boldsymbol{\Omega}\left(\boldsymbol{\omega}^b_{nb}\right)\boldsymbol{q}^n_b \tag{14}$$

based on the underlying assumption above that NED can be considered inertial. Moreover,

$$\boldsymbol{f}^b_{nb} = \boldsymbol{R}^\intercal_{nb}(\boldsymbol{q}^n_b)\dot{\boldsymbol{v}}^n_{nb} - \boldsymbol{R}^\intercal_{nb}(\boldsymbol{q}^n_b)\boldsymbol{g}^n_b \tag{15}$$

represent the specific force.

III. Sensor Suite

The PARS-based navigation system relies on measurement of a series of physical quantities, whose measurement principles and equations are presented in the following section.

A. Phased Array Radio System Positioning

The primary functionality of the PARS is communication, nevertheless, the system can also be used as a positioning system. By observing the phase difference of the incoming signal between the different antenna elements in the radio array, the azimuth and elevation of the UAV can be observed, in the ground radio's frame of reference, $\{r\}$. This is known as the direction-of-arrival (DOA) problem [12], which has several known solutions [13], [14]. Through timing of the transmission time and subtraction of the internal processing time, a measurement of the geometric range between the PARS ground station to the UAV is found.

After having rotated the PARS range, elevation and bearing measurements from the $\{r\}$-frame to the $\{n\}$-frame, the measurements can be used to calculate the relative position of the UAV in a local Earth-fixed frame. When using an Earth-fixed, non-rotating, local NED frame, as in this paper, the range, azimuth and elevation measurements are related to the UAV position, through the radio coordinate system $\{r\}$ using,

$$y_\rho = \rho_u + \varepsilon_\rho, \tag{16}$$

$$y_\Psi = \Psi_u + \varepsilon_\Psi, \tag{17}$$

$$y_\alpha = \alpha_u + \varepsilon_\alpha, \tag{18}$$

where

$$\rho_u = \|\boldsymbol{p}^r_{\text{PARS}}\|_2, \tag{19}$$

$$\Psi_u = \arctan\left(\frac{p^r_{rb,y}}{p^r_{rb,x}}\right), \tag{20}$$

$$\alpha_u = \arctan\left(\frac{-p^r_{rb,z}}{\bar{\rho}_u}\right) \tag{21}$$

with

$$\|\boldsymbol{p}^r_{\text{PARS}}\|_2 = \sqrt{\left(p^r_{rb,x}\right)^2 + \left(p^r_{rb,y}\right)^2 + \left(p^r_{rb,z}\right)^2},$$

while $\varepsilon_\star \sim \mathcal{N}(0, \sigma^2_\star)$ represents zero-mean Gaussian noise. A physical intuition of the geometric range ρ_u, elevation angle α_u and azimuth angle Ψ_u, given in the $\{r\}$-frame, can be seen in Fig. 2. Moreover, the relationships of (19)–(21) are similar to those in [15, Ch. 13.6.2.2], used for radar tracking of aircraft, and can be derived from

$$\boldsymbol{p}^r_{\text{PARS}} = \begin{pmatrix} p^r_{rb,x} \\ p^r_{rb,y} \\ p^r_{rb,z} \end{pmatrix} = \begin{pmatrix} \rho_u \cos(\Psi_u)\cos(\alpha_u) \\ \rho_u \sin(\Psi_u)\cos(\alpha_u) \\ -\rho_u \sin(\alpha_u)) \end{pmatrix}, \tag{22}$$

according to Fig. 2. Following [16, Section 1.7.4], the bias arising from the nonlinear mapping of the azimuth and

elevation angle measurement noise into Cartesian coordinates can be corrected for by

$$\bar{\boldsymbol{p}}^r_{\text{PARS}} = \begin{pmatrix} b_\Psi^{-1} b_\alpha^{-1} y_\rho \cos(y_\Psi)\cos(y_\alpha) \\ b_\Psi^{-1} b_\alpha^{-1} y_\rho \sin(y_\Psi)\cos(y_\alpha) \\ -b_\alpha^{-1} y_\rho \sin(y_\alpha) \end{pmatrix}, \tag{23}$$

in which $b_\Psi = \mathbb{E}[\cos(\varepsilon_\Psi)] = e^{-\sigma_\Psi^2/2}$ and $b_\alpha = \mathbb{E}[\cos(\varepsilon_\alpha)] = e^{-\sigma_\alpha^2/2}$. Based on (23), the PARS position is given in the $\{n\}$ frame with

$$\boldsymbol{p}^n_{\text{PARS}} = \boldsymbol{R}^n_r(\boldsymbol{\Theta}_{\text{PARS}})\bar{\boldsymbol{p}}^r_{\text{PARS}}, \tag{24}$$

where $\boldsymbol{\Theta}_{\text{PARS}}$ represent rotation angles of $\{r\}$ about $\{n\}$, obtained during calibration of the PARS ground antenna [4].

B. Inertial Measurement Unit

A simplified measurement model of an IMU [3], providing specific force and angular rate sensor (ARS) measurements, is given as

$$\boldsymbol{f}^b_{\text{IMU}} = \boldsymbol{f}^b_{nb} + \boldsymbol{b}^b_{\text{acc}} + \boldsymbol{\varepsilon}^b_{\text{acc}} \tag{25}$$
$$\boldsymbol{\omega}^b_{\text{IMU}} = \boldsymbol{\omega}^b_{nb} + \boldsymbol{b}^b_{\text{ars}} + \boldsymbol{\varepsilon}^b_{\text{ars}} \tag{26}$$

where $\boldsymbol{b}^b_\star$ represent the ACC and the ARS biases. $\boldsymbol{\varepsilon}^b_\star$ represent zero-mean noise.

IV. The navigation System

The PARS-based navigation system itself consists of an INS, whose purpose is to propagate the system dynamics given the new IMU measurement, and a multiplicative extended Kalman filter (MEKF), which is used to correct the INS' state, $\boldsymbol{x}_{\text{ins}}$, using an indirect feedback filter implementation [17], [11, Ch. 5.10.5.3]. Using this approach the INS state is steered towards the true state, $\boldsymbol{x}$ by estimating the error state $\delta\boldsymbol{x}$, using

$$\boldsymbol{x} = \boldsymbol{x}_{\text{ins}} \oplus \delta\boldsymbol{x}, \tag{27}$$

where $\oplus$ represents the + or the $\otimes$ operator, depending on the state definition. As a result $\boldsymbol{x}_{\text{ins}} \to \boldsymbol{x}$ when the error state goes to zero/the identity quaternion. The chosen state vector of the INS was

$$\boldsymbol{x}_{\text{ins}} = \left(\boldsymbol{p}^n_{nb,\text{ins}}; \boldsymbol{v}^n_{nb,\text{ins}}; \boldsymbol{q}^n_{b,\text{ins}}; \boldsymbol{b}^b_{\text{acc,ins}}; \boldsymbol{b}^b_{\text{ars,ins}}\right). \tag{28}$$

By mimicking the kinematics of Section II-D we obtained the follow kinematic model

$$\dot{\boldsymbol{p}}^n_{nb,\text{ins}} = \boldsymbol{v}^n_{nb,\text{ins}} \tag{29}$$
$$\dot{\boldsymbol{v}}^n_{nb,\text{ins}} = \boldsymbol{R}_{nb}(\boldsymbol{q}^n_{b,\text{ins}})\left(\boldsymbol{f}^b_{\text{IMU}} - \boldsymbol{b}^b_{\text{acc,ins}}\right) + \boldsymbol{g}^n_b \tag{30}$$
$$\dot{\boldsymbol{q}}^n_{b,\text{ins}} = \frac{1}{2}\boldsymbol{\Omega}\left(\boldsymbol{\omega}^b_{\text{ars}} - \boldsymbol{b}^b_{\text{ars,ins}}\right)\boldsymbol{q}^n_{b,\text{ins}} \tag{31}$$
$$\dot{\boldsymbol{b}}^b_{\text{acc,ins}} = -\boldsymbol{T}^{-1}_{\text{acc}}\boldsymbol{b}^b_{\text{acc,ins}} \tag{32}$$
$$\dot{\boldsymbol{b}}^b_{\text{ars,ins}} = -\boldsymbol{T}^{-1}_{\text{ars}}\boldsymbol{b}^b_{\text{ars,ins}} \tag{33}$$

where $\boldsymbol{T}_\star$ are time constants. These equations can be mechanized in discrete time using any integration method of choice. Exact integration methods concerting the quaternion integration can be found in [11], [18].

A. Multiplicative extended Kalman filter

The state vector of the MEKF, given as

$$\delta\boldsymbol{x} = (\delta\boldsymbol{p}; \delta\boldsymbol{v}; \delta\boldsymbol{a}; \delta\boldsymbol{b}_{\text{acc}}; \delta\boldsymbol{b}_{\text{ars}}), \tag{34}$$

where $\delta\boldsymbol{a}$ represents the 3D attitude error, is calculated for every new aiding measurement using a standard error state Kalman filter implementation [3], [11]. After every iteration of the MEKF, the INS states with linear error states corrections are updated using

$$\boldsymbol{\xi}^n_{n\hat{b},\text{ins}}[k] \leftarrow \boldsymbol{\xi}^n_{n\hat{b},\text{ins}}[k] + \delta\hat{\boldsymbol{\xi}}[k], \tag{35}$$

where $\boldsymbol{\xi}$ is a placeholder for the position, velocity and the biases. Moreover, the attitude is corrected using

$$\delta\boldsymbol{q}(\delta\hat{\boldsymbol{a}}[k]) = \frac{1}{16 + \hat{\boldsymbol{a}}^\intercal[k]\hat{\boldsymbol{a}}[k]}\begin{pmatrix} 16 - \delta\hat{\boldsymbol{a}}^\intercal[k]\delta\hat{\boldsymbol{a}}[k] \\ 8\cdot\delta\hat{\boldsymbol{a}}[k] \end{pmatrix}, \tag{36}$$
$$\boldsymbol{q}^n_{b,\text{ins}}[k] \leftarrow \boldsymbol{q}^n_{\hat{b},\text{ins}}[k] \otimes \delta\boldsymbol{q}(\delta\hat{\boldsymbol{a}}[k]). \tag{37}$$

similar to [8]. After the INS states have been corrected, the MEKF state is reset to zero

$$\delta\hat{\boldsymbol{x}}[k] \leftarrow \boldsymbol{0}_{n\times 1}. \tag{38}$$

For every new IMU measurement, at time $t[k]$ at time index k the covariance is propagated forward in time according to

$$\boldsymbol{P}^-[k+1] \leftarrow \boldsymbol{A}_d[k]\boldsymbol{P}^+[k]\boldsymbol{A}^\intercal_d[k] + \boldsymbol{Q}_d[k]. \tag{39}$$

The $\boldsymbol{A}_d[k]$ and $\boldsymbol{Q}_d[k]$ can be calculated based on the continuous-time model

$$\delta\dot{\boldsymbol{x}} = \boldsymbol{A}(t)\delta\boldsymbol{x} + \boldsymbol{B}(t)\boldsymbol{w} \tag{40}$$

where $\boldsymbol{A}(t)$ and $\boldsymbol{B}(t)$, based on the error state parameterization presented found in Appendix I. $\boldsymbol{Q} = E[\boldsymbol{w}\boldsymbol{w}^\intercal]$ is the covariance of

$$\boldsymbol{w} = \left(\boldsymbol{w}^b_{\text{acc}}; \boldsymbol{w}^b_{\text{ars}}; \boldsymbol{w}^b_{b,\text{acc}}; \boldsymbol{w}^b_{b,\text{ars}}\right). \tag{41}$$

The $\boldsymbol{A}(t)$, $\boldsymbol{B}(t)$ and $\boldsymbol{Q}(t)$ matrices can then be used to calculate the $\boldsymbol{A}_d[k]$ and $\boldsymbol{Q}_d[k]$ matrices using e.g. van Loan's algorithm, [19] or using standard discretization techniques [20, Ch. 4.2.1].

B. PARS measurements equation

The linear position $\boldsymbol{y}_{\text{pars}} = \boldsymbol{p}^n_{\text{pars}}$ measurement is calculated using (24) such that a linear measurement matrix

$$\boldsymbol{C} = \begin{pmatrix} \boldsymbol{I}_3 & \boldsymbol{0}_{3\times3} & \boldsymbol{0}_{3\times3} & \boldsymbol{0}_{3\times3} & \boldsymbol{0}_{3\times3}, \end{pmatrix} \tag{42}$$

can be applied in the error state Kalman filter. This, however, requires a mapping of the covariance from spherical coordinates to Cartesian coordinates. This is done by linearizing the measurement $\boldsymbol{y}_{\text{pars}}$ w.r.t. to the measurement noise [16, Ch. 1.7], $\boldsymbol{\varepsilon} = \begin{pmatrix} \varepsilon_\rho; & \varepsilon_\Psi; & \varepsilon_\alpha \end{pmatrix}$ in order to calculate a mapping Jacobian matrix,

$$\boldsymbol{M} = \frac{\partial \boldsymbol{y}_{\text{pars}}}{\partial \boldsymbol{\varepsilon}} = \begin{pmatrix} m_{11} & m_{12} & m_{13} \\ m_{21} & m_{22} & m_{23} \\ m_{31} & m_{32} & m_{33} \end{pmatrix}, \tag{43}$$

where

$$
\begin{aligned}
m_{11} &= \frac{\mathrm{c}(y_\Psi)\mathrm{c}(y_\alpha)}{b_\Psi b_\alpha} & m_{12} &= \frac{-y_\rho \mathrm{c}(y_\alpha)\mathrm{s}(y_\Psi)}{b_\Psi b_\alpha} \\
m_{13} &= \frac{-y_\rho \mathrm{c}(y_\Psi)\mathrm{s}(y_\alpha)}{b_\Psi b_\alpha} & m_{21} &= \frac{\mathrm{c}(y_\alpha)\mathrm{s}(y_\Psi)}{b_\Psi b_\alpha} \\
m_{22} &= \frac{y_\rho \mathrm{c}(y_\Psi)\mathrm{c}(y_\alpha)}{b_\Psi b_\alpha} & m_{23} &= \frac{-y_\rho \mathrm{s}(y_\Psi)\mathrm{s}(y_\alpha)}{b_\Psi b_\alpha} \\
m_{31} &= \frac{\mathrm{s}(y_\alpha)}{b_\alpha} & m_{32} &= 0 \\
m_{33} &= \frac{-y_\rho \mathrm{c}(y_\alpha)}{b_\alpha}.
\end{aligned}
$$

and $\mathrm{s}(\star) := \sin(\star)$, $\mathrm{c}(\star) := \cos(\star)$. The $\boldsymbol{M}$ matrix is then applied taking

$$\boldsymbol{R}_{\text{pars}}(t) = \boldsymbol{R}_r^n \boldsymbol{M}(t) \boldsymbol{R}_s(t) \boldsymbol{M}^\intercal(t) \boldsymbol{R}_n^r. \tag{44}$$

in order to calculate the linearized measurement covariance matrix $\boldsymbol{R}_{\text{pars}}$, in the $\{n\}$ frame, where $\boldsymbol{R}_s(t)$ represents the covariance of $\boldsymbol{\varepsilon}$ given in spherical coordinates.

C. Outlier rejection

As seen in e.g. [7], the PARS is susceptible to noise, particularly reflections. This comes from the fact that the PARS currently is optimized for communication, not navigation, which causes the beam to travel in the path that gives the best communication, not necessarily the best navigation. To avoid degradation of the PVA estimates from bad PARS measurements, outlier rejection can be added.

Given the normalized residual [21, Section 7.6.1]

$$\epsilon = (\boldsymbol{C}\boldsymbol{P}^-\boldsymbol{C}^\intercal + \boldsymbol{R})^{-\frac{1}{2}}(\boldsymbol{y} - \boldsymbol{C}), \tag{45}$$

in which the central limit theorem motivates the Gaussian approximation, the null hypothesis of the measurement being an inlier is discarded if the test statistic

$$T(\boldsymbol{y}^r_{\text{pars}}) = (\boldsymbol{y}^r_{\text{pars}} - \boldsymbol{C}\boldsymbol{x})^\intercal (\boldsymbol{C}\boldsymbol{P}^-\boldsymbol{C}^\intercal + \boldsymbol{R})^{-1}(\boldsymbol{y}^r_{\text{pars}} - \boldsymbol{C}\boldsymbol{x}) \sim \chi^2_1 \tag{46}$$

is above some limit χ^2_α.

V. Practical aspects

Realization of a PARS for real-time use also calls for integration of sensors and implementation of the INS algorithms in an real-time capable environment, a process whose details are specified in the following subsections.

A. Hardware

An overview of the hardware used in the experiment, and its interconnection, is showed in Fig. 6. The IMU used in the experiments was a Sensonor STIM300, a light-weight, tactical grade, high-performance MEMS-based sensor, configured to output incremental velocity and incremental angles at 250 Hz.

To provide a high-accuracy position reference, used as a basis for evaluating the performance of the PARS-based position estimates, the payload was also equipped with a Ublox Neo-M8T GNSS receiver. The receiver was configured to output raw GNSS observables, which, in combination with correction data from a ground station through RTKLIB, were used to derive a high accuracy real-time kinematics (RTK) positioning solution.

Fig. 3: Radionor CRE2-189 ground station antenna

Furthermore, a SenTiBoard [22] was used to synchronize and timestamp the IMU and GNSS measurements for post-process analysis and to ease the integration of the IMU measurements into one Odroid XU4, used as on-board computer.

The on-board computer was also connected to a Pixhawk 3 Pro autopilot running ArduCopter flight control software. Internally, the autopilot also has a GNSS, magnetometer, barometer and a low-quality IMU, used in its internal INS[1]. The raw measurements and INS states from the autopilot are recorded to be used as a reference. Furthermore, the autopilot's GPS-aided INS states were used in the closed-loop feedback, as opposed to the PARS-based estimates, as a safety precaution.

The on-board computer is connected to the UAV-side PARS, to send telemetry data to the ground station, and to receive commands and PARS measurements. The PARS used in these experiments was the Radionor CRE2-189 and CRE2-144-M2-SMA, seen in Fig. 3 and Fig. 4 respectively. The CRE2-189 is a ground radio with 8x8 antenna elements,, and covering a 90° frustum both in elevation and in azimuth with an root mean square error of 0.1° in each axis. The CRE2-144-M2-SMA is the $146 \times 78 \times 43$mm, 295 g UAV onboard counterpart, which has four SMA antenna connectors. In addition to providing the link between the UAV and the ground station, the UAV PARS also works as a relay for communication from other nodes in the network that not necessarily have radio line-of-sight to the ground station. This combination of ground and UAV radios allow for ranges of up to 114 km, when transmission rates are limited to 0.5 Mbit/s.

All the equipment was mounted in a Nordic Unmanned

[1] Among the different INS solutions available in the ArduPlane codebase, the EKF2 was used, as it currently is the default version.

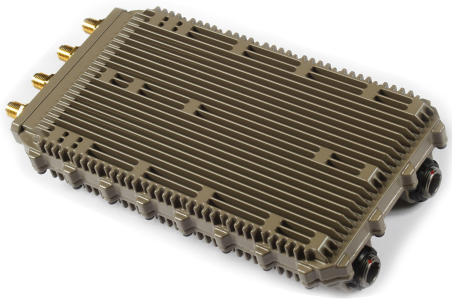

Fig. 4: Radionor CRE2-144-M2-SMA radio module

Fig. 5: Nordic Unmanned Camflight BG-200 HL UAV

Camflight BG-200 HL UAV, manufactured and operated by Nordic Unmanned. This is a 140 cm-diameter octocopter designed for high-precision mapping, seen in Fig. 5.

B. Software

The PARS INS was implemented in DUNE Unified Navigation Environment [23], a robotic middleware written in C++. DUNE also supports a playback of previously recorded data, to simplify the tuning process and to allow for testing of new features without the need for new flight time. This runs in Ubuntu Mate linux on the onboard computer.

C. Calibration

Since the PARS only provides a position measurement relative to its ground station ($\{r\}$-frame), pre-flight calibration to obtain the full pose of the ground station antenna relative to the $\{n\}$-frame is crucial to obtain accurate absolute position estimates. While the full pose consists of the geodetic position and the roll-, pitch- and yaw angles, only the position and yaw angle was considered in the presented experiment, since the effects of roll and pitch misalignment are difficult to separate from PARS measurement noise. The position of the PARS ground station antenna was surveyed using a GNSS receiver, while the heading of the antenna was adjusted so that the PARS-based position estimates and the GNSS-based position estimates from the autopilot aligned. In a scenario where the ground station experiences malicious GNSS attacks, a GNSS antenna with heavy shielding on its sides could be used, since most GNSS attacks come from land-based units and since attackers from above are easier to immobilize. For a completely GNSS-free solution, the ground station position can be found from a map, e.g. using a particle filter and terrain information or odometry [24], or by using feature matching [3, Chapter 11].

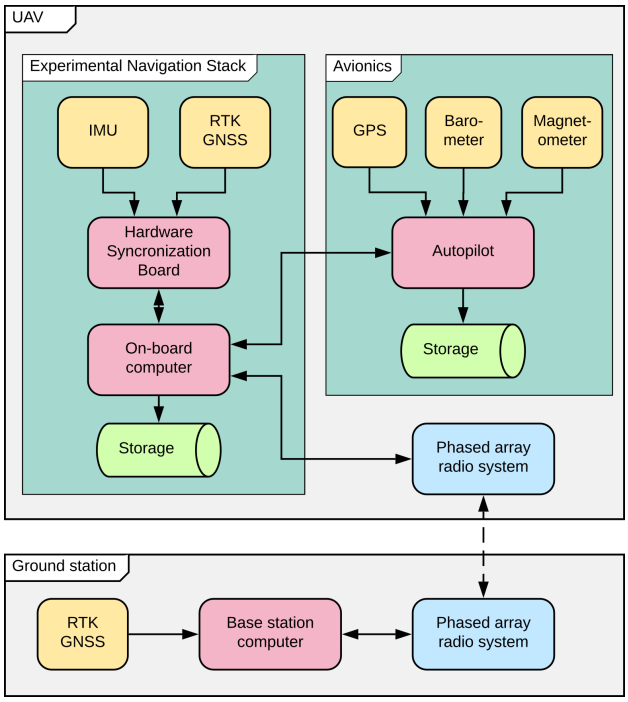

Fig. 6: System overview

TABLE I: Attitude Statistics

	Roll [°]	**Pitch** [°]	**Yaw** [°]	**Norm** [°]
ME:	0.45	-1.20	-0.46	1.36
AME:	0.95	1.65	4.18	4.59
STD:	1.42	1.75	7.24	7.58
RMSE:	1.49	2.12	7.25	7.70

For obtaining the heading of the ground station antenna, there are also a variety of options [25], notably [26] where attitude is determined from a camera and a digital surface model with a standard deviation of 0.018° in heading.

VI. Results

The experiment presented in this section was a part of a commercial demonstration by Radionor Communications, in the northern parts of Norway. The main objectives were to relay the video and audio feed from two mobile cameras through the UAV, whose GNSS-free position estimate was displayed on a map in a command center along with the video/audio feed. Numerical values for the covariance matricies $\boldsymbol{Q}$ and $\boldsymbol{R}$ are found in Section I-A, while $\chi^2_\alpha = 7$ was chosen as the outlier rejection threshold.

The results from the experiment are visually presented in Fig. 7, while mean-error (ME), absolute mean-error (AME), standard deviation (STD) and root mean square error (RMSE) statistics are shown in Table I, Table II and Table III, for attitude, position and velocity, respectively.

In Fig. 7a, the attitude from the PARS-aided INS is compared to the attitude and heading reference (AHRS) of the

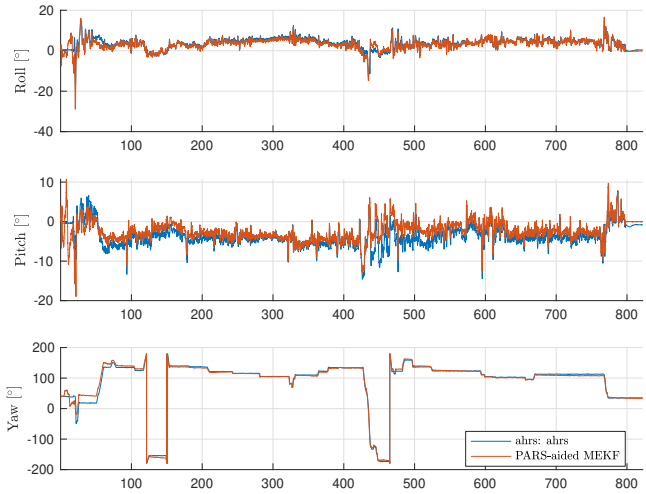

(a) Attitude, compared to autopilot reference

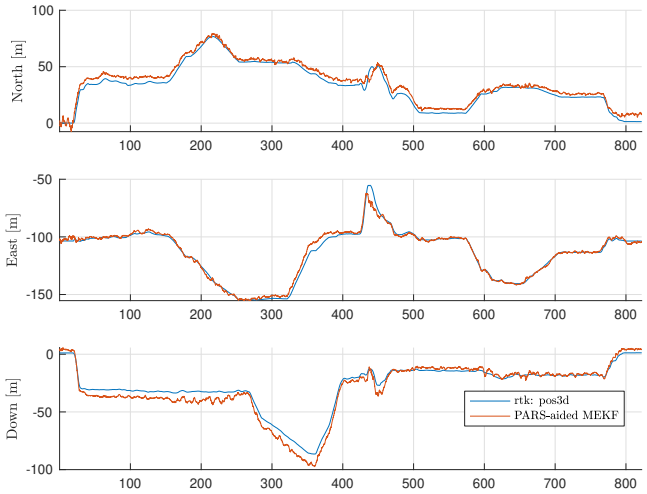

(b) NED position, compared to RTK GNSS reference

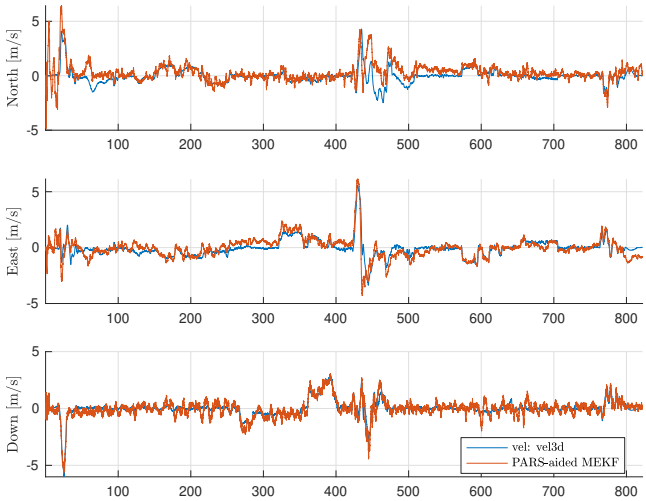

(c) NED velocity, compared to autopilot reference

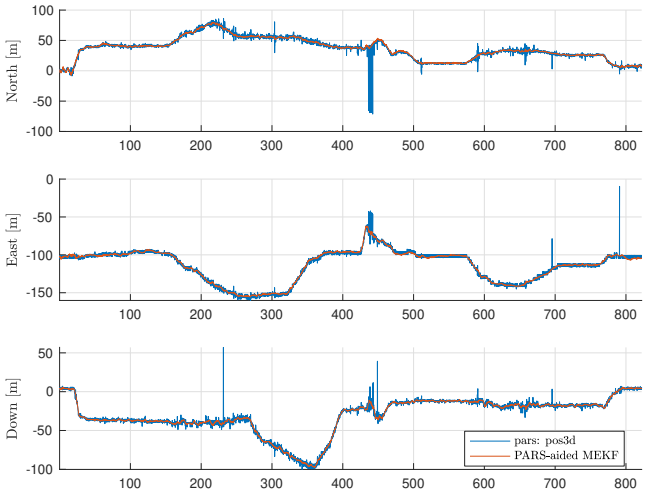

(d) Raw PARS NED position, compared to RTK GNSS reference

Fig. 7: North-Down plot with attitude

TABLE II: Position Statistics PARS-aided INS

	North [m]	**East** [m]	**Down** [m]	**Norm** [m]
ME:	-3.43	-0.59	2.56	4.32
AME:	3.64	1.65	4.02	5.67
STD:	2.11	2.56	4.18	5.33
RMSE:	4.03	2.63	4.90	6.86

TABLE III: Velocity Statistics PARS-aided INS

	North [m/s]	**East** [m/s]	**Down** [m/s]	**Norm** [m/s]
ME:	-0.32	-0.04	0.04	0.32
AME:	0.49	0.38	0.31	0.69
STD:	0.70	0.54	0.40	0.97
RMSE:	0.77	0.55	0.40	1.02

autopilot. Seeing as the autopilot is low-cost, and thus based on low accuracy components, it should not be considered a ground truth, especially as it relies on a magnetic compass which is vulnerable to magnetic disturbances. However, it is a well established navigation solution for closed-loop flight, and is therefore considered an appropriate reference. Table I shows that the AHRS and the PARS-aided INS are reasonably similar. The majority of the attitude error is the yaw for the first 50 s. However, yaw is also the axis in which the AHRS accuracy is believed to be the worst, since the gravity vector measured by the accelerometer is independent of the yaw angle. This leaves one less sensor to determine yaw, compared to roll and pitch. Furthermore, the accuracy of both the AHRS and the PARS-aided INS estimates are believed to improve in flights with more agile maneuvers.

Comparing to a standalone RTK GNSS position estimate, in Table II, the norm of the position RMSE for the PARS-aided INS is comparable to that of a consumer grade GPS receiver, when operating at this range from the ground station. When comparing Fig. 7b to Fig. 7d, which also includes the position calculated directly from the PARS measurements, it is apparent that the presented INS is able to reject most of the outliers, and obtain smoother position estimates.

Studying Fig. 7c one can see that the PARS-aided INS tracks the velocity of the autopilot well, except for a short time window around 450 seconds. This deviation probably stems from one or more measurements, that should have been rejected as outliers, were used in correcting the INS. When the inlier measurement again were used for corrections, the velocity recovered. Looking Table III one can also see that the velocity estimates were accurate compared to the autopilot velocity.

VII. Conclusion

Aiding a MEMS-based INS with PARS-based spherical position measurements in an MEKF, has through field tests proven to be a reasonable alternative for obtaining position, velocity and attitude estimates of a small multirotor unmanned aerial vehicle. When compared to a standalone RTK GNSS reference, the position norm RMSE of the presented PARS-aided INS was 6.86 m, which is comparable to the position estimates from consumer grade GNSS-receivers. The presented PARS makes the unmanned aerial vehicle independent of GNSS and compass, but the position and attitude of the ground station antenna, which is essential for obtaining absolute position estimates in the $\{n\}$-frame, were found using GNSS. Methods to obtain completely GNSS- and compass-free estimates have been suggested.

Appendix I
MEKF Matrices

The error-state system matrices, based on the four times MRP attitude error paramtrization can be given as, based on $\boldsymbol{q}_b^n = \boldsymbol{q}_{b,\text{ins}}^n \otimes \delta\boldsymbol{q}$,

$$\boldsymbol{A}(t) = \begin{pmatrix} \boldsymbol{0}_{3\times3} & \boldsymbol{I}_3 & \boldsymbol{0}_{3\times3} & \boldsymbol{0}_{3\times3} & \boldsymbol{0}_{3\times3} \\ \boldsymbol{0}_{3\times3} & \boldsymbol{0}_{3\times3} & \boldsymbol{V}_a & \boldsymbol{V}_{\text{acc}} & \boldsymbol{0}_{3\times3} \\ \boldsymbol{0}_{3\times3} & \boldsymbol{0}_{3\times3} & \boldsymbol{A}_a & \boldsymbol{0}_{3\times3} & \boldsymbol{A}_{\text{ars}} \\ \boldsymbol{0}_{3\times3} & \boldsymbol{0}_{3\times3} & \boldsymbol{0}_{3\times3} & -\boldsymbol{T}_{\text{acc}}^{-1} & \boldsymbol{0}_{3\times3} \\ \boldsymbol{0}_{3\times3} & \boldsymbol{0}_{3\times3} & \boldsymbol{0}_{3\times3} & \boldsymbol{0}_{3\times3} & -\boldsymbol{T}_{\text{ars}}^{-1} \end{pmatrix} \in \mathbb{R}^{15\times15}, \quad (47)$$

$$\boldsymbol{B}(t) = \begin{pmatrix} \boldsymbol{0}_{3\times3} & \boldsymbol{0}_{3\times3} & \boldsymbol{0}_{3\times3} & \boldsymbol{0}_{3\times3} \\ -\boldsymbol{R}_{n\hat{b}}(\boldsymbol{q}_{\hat{b},\text{ins}}^n) & \boldsymbol{0}_{3\times3} & \boldsymbol{0}_{3\times3} & \boldsymbol{0}_{3\times3} \\ \boldsymbol{0}_{3\times3} & -\boldsymbol{I}_3 & \boldsymbol{0}_{3\times3} & \boldsymbol{0}_{3\times3} \\ \boldsymbol{0}_{3\times3} & \boldsymbol{0}_{3\times3} & \boldsymbol{I}_3 & \boldsymbol{0}_{3\times3} \\ \boldsymbol{0}_{3\times3} & \boldsymbol{0}_{3\times3} & \boldsymbol{0}_{3\times3} & \boldsymbol{I}_3 \end{pmatrix} \in \mathbb{R}^{15\times12}, \quad (48)$$

where

$$\begin{aligned} \boldsymbol{V}_a &= -\boldsymbol{R}_{n\hat{b}}(\boldsymbol{q}_{\hat{b},\text{ins}}^n)\,\boldsymbol{S}\left(\boldsymbol{f}_{\text{imu}}^b - \boldsymbol{b}_{\text{acc,ins}}^{\hat{b}}\right), \\ \boldsymbol{V}_{\text{acc}} &= -\boldsymbol{R}_{n\hat{b}}(\boldsymbol{q}_{\hat{b},\text{ins}}^n), \\ \boldsymbol{A}_a &= -\boldsymbol{S}\left(\boldsymbol{\omega}_{\text{imu}}^b - \boldsymbol{b}_{\text{ars,ins}}^{\hat{b}}\right), \\ \boldsymbol{A}_{\text{ars}} &= -\boldsymbol{I}_3. \end{aligned}$$

A. Tuning

The following numerical values where used for the covariance matrices $\boldsymbol{Q}$ and $\boldsymbol{R}$ in the experiment

$$\boldsymbol{Q} = \begin{pmatrix} q_{\text{acc}}^2 & 0 & 0 & 0 \\ 0 & q_{\text{ars}}^2 & 0 & 0 \\ 0 & 0 & q_{\text{acc bias}}^2 & 0 \\ 0 & 0 & 0 & q_{\text{ars bias}}^2 \end{pmatrix} \quad (49)$$

$$\boldsymbol{R} = \begin{pmatrix} r_{\text{range}}^2 & 0 & 0 \\ 0 & r_{\text{azi}}^2 & 0 \\ 0 & 0 & r_{\text{elev}}^2 \end{pmatrix} \quad (50)$$

where the diagonal terms are set to $q_{\text{acc}} = 47.85\,\text{m/s}^2$, $q_{\text{ars}} = 5.35\times10^{-7}\,\text{rad/s}$, $q_{\text{acc bias}} = 4.91\times10^{-3}\,\text{m/s}^2$, $q_{\text{ars bias}} = 1.74\times10^{-7}\,\text{rad/s}$, $r_{\text{azi}} = r_{\text{elev}} = 3.49\times10^{-2}\,\text{rad}$ and $r_{\text{range}} = 15.0\,\text{m}$.

Acknowledgment

The authors thank Jon Are Kolstad, Øystein Pedersen and Inge Aune Paulsen at Radionor Communications for allowing us to use the PARS equipment their support with the PARS positioning system. Furthermore we thank Thomas André Olsen from Nordic Unmanned for piloting the UAV.

References

[1] A. Pinker and C. Smith, "Vulnerability of the GPS signal to jamming," *GPS Solutions*, vol. 3, no. 2, pp. 19–27, 1999.

[2] A. J. Kerns, D. P. Shepard, J. A. Bhatti, and T. E. Humphreys, "Unmanned aircraft capture and control via GPS spoofing," *Journal of Field Robotics*, vol. 31, no. 4, pp. 617–636, 2014.

[3] P. D. Groves, *Principles of GNSS, Inertial, and Multisensor Integrated Navigation Systems*, 2nd ed. Artech House, 2013.

[4] S. M. Albrektsen, A. Sægrov, and T. A. Johansen, "Navigation of uav using phased array radio," in *Workshop on Research, Education and Development of Unmanned Aerial Systems (RED UAS)*, 3-.5 Oct. 2017, pp. 138–143.

[5] V. E. Hovstein, A. Sægrov, and T. A. Johansen, "Experiences with coastal and maritime UAS BLOS operation with phased-array antenna digital payload data link," in *Proc. International Conference Unmanned Aircraft Systems (ICUAS)*, Orlando, FL, 27–30 May 2014, pp. 262–266.

[6] S. M. Albrektsen, T. H. Bryne, and T. A. Johansen, "Phased array radio system aided inertial navigation for unmanned aerial vehicles," in *Proc. of the IEEE Aerospace Conference*, Big Sky, Montana, March 3–10 2018, pp. 1–11.

[7] ——, "Robust and secure uav navigation using gnss, phased-array radiosystem and inertial sensor fusion," in *2nd IEEE Conference on Control Technology and Applications*, Copenhagen, Denmark, Aug. 21–24 2018, pp. 1338–1345.

[8] F. L. Markley, "Attitude error representation for kalman filtering," *Journal of Guidance, Control, and Dynamics*, vol. 26, no. 2, pp. 311–317, March 2003.

[9] T. I. Fossen, *Handbook of Marine Craft Hydrodynamics and Motion Control*. John Wiley & Sons, Ltd., 2011.

[10] K. Gade, *Inertial Navigation – Theory and Applications*. Doctral dissertation, Norwegian University of Science and Technology (NTNU), January 2018.

[11] J. A. Farrell, *Aided Navigation: GPS with High Rate Sensors*. McGraw-Hill, 2008.

[12] H. Krim and M. Viberg, "Two decades of array signal processing research: the parametric approach," *IEEE Signal Processing Magazine*, vol. 13, no. 4, pp. 67–94, Jul 1996.

[13] R. Roy and T. Kailath, "ESPRIT-estimation of signal parameters via rotational invariance techniques," *IEEE Transactions on Acoustics, Speech, and Signal Processing*, vol. 37, no. 7, pp. 984–995, Jul 1989.

[14] R. Schmidt, "Multiple emitter location and signal parameter estimation," *IEEE Transactions on Antennas and Propagation*, vol. 34, no. 3, pp. 276–280, Mar 1986.

[15] D. H. Titterton and J. L. Weston, *Strapdown inertial navigation technology*, 2nd ed. Institution of Electrical Engineers and American Institute of Aeronautics and Astronautics, 2004.
[16] Y. Bar-Shalom, P. K. Willett, and X. Tian, *Tracking and Data Fusion: A Handbook of Algorithms*. YBS Publishing, 2011.
[17] S. Roumeliotis, G. Sukhatme, and G. Bekey, "Circumventing dynamic modeling: Evaluation of the error-state kalman filter applied to mobile robot localization," in *IEEE International Conference on Robotics and Automation*, Detroit, Michigan, May 10-15 1999, pp. 1656–1663.
[18] T. H. Bryne, J. M. Hansen, R. H. Rogne, N. Sokolova, T. I. Fossen, and T. A. Johansen, "Nonlinear observers for integrated INS/GNSS navigation – Implementation aspects," *IEEE Control Systems Magazine*, vol. 37, no. 3, pp. 59–86, 2017.
[19] C. F. van Loan, "Computing integrals involving the matrix exponential," *IEEE Trans. Automatic Control*, vol. AC–23, no. 3, pp. 395–404, 1978.
[20] C.-T. Chen, *Linear system theory and design*. Oxford University Press, Inc., 1998.
[21] F. Gustafsson, *Statistical Sensor Fusion*, 2nd ed. Studentlitteratur, 2012.
[22] M. S. Albrektsen and T. A. Johansen, "User-configurable timing and navigation for UAVs," *Sensors*, vol. 18, no. 8, pp. 1–27, 2018.
[23] J. Pinto, P. S. Dias, R. Martins, J. Fortuna, E. Marques, and J. Sousa, "The lsts toolchain for networked vehicle systems," in *2013 MTS/IEEE OCEANS-Bergen*. IEEE, 2013, pp. 1–9.
[24] F. Gustafsson, "Particle filter theory and practice with positioning applications," *IEEE Aerospace and Electronic Systems Magazine*, pp. 53–82, 2010.
[25] K. Gade, "The seven ways to find heading," *The Journal of Navigation*, pp. 1–16, 2016.
[26] C. D. Rodin, T. A. Johansen, and A. Stahl, "Skyline based camera attitude estimation using a digital surface model," in *2018 IEEE 15th International Workshop on Advanced Motion Control (AMC)*. IEEE, 2018, pp. 306–313.